

Synthesis, surface analysis of NiO doped Li nanoparticles for advanced photocatalytic application in waste water treatment

E. Tamil Selvi^a, R. Uthrakumar^{a,*}, C. Inmozhi^b, K. Kaviyarasu^{c,d}

^a*Department of Physics, Govt. Arts College (Autonomous), Salem - 636007, Tamil Nadu, India*

^b*Department of Physics, Govt. Arts College for Women, Salem - 636008, Tamil Nadu, India*

^c*UNESCO-UNISA Africa Chair in Nanosciences/Nanotechnology Laboratories, College of Graduate Studies, University of South Africa (UNISA), Muckleneuk Ridge, PO Box 392, Pretoria, South Africa*

^d*Nanosciences African Network (NANOAFNET), Materials Research Group (MRG), iThemba LABS-National Research Foundation (NRF), 1 Old Faure Road, 7129, PO Box 722, Somerset West, Western Cape Province, South Africa*

Present work that maximizes how lithium ions (Li) acting as a dopant affect the structure, morphology, optical, and electrical characteristics of nickel oxide (NiO) nanoparticles by co-precipitation method. It also reveals the face-centered cubic (FCC) structure of the yield material, as also evident by Transmission electron microscopy (TEM) results. Li ion observed TEM studies evident the size reductions of the NiO nanoparticles after capping processes. FTIR and UV-vis absorption spectroscopy reveals the functional behaviour of the composite elements and confirms the elemental existence. Photocatalytic observations reveal the dye degradation efficiency of NiO-Li composite nearly 96% against visible light irradiations.

(Received September 1, 2023; Accepted January 15, 2024)

Keywords: NiO nanoparticles, Organic dye, UV-Visible, Photocatalytic performance, Transmission electron microscopy, Advanced oxidation process.

1. Introduction

Recently, there has been a sharp increase in interest in the synthesis of nanoparticles, which has led to their widespread production [1]. Numerous research over the last few decades imply that because nanomaterials have smaller particles than traditional materials, their reactivity responses may be separate from or even outperformed. Particularly, when the material is incorporated with the foreign element of different nature, the material characteristics are found to be modified drastically. In such case of materials having nanoparticles, these reported property modifications will be entirely new, incomparable to their parent materials. Recent research works showing interests on developing such nanocomposite materials with newer and novel characteristics. Due to its unique functional properties and significance in a wide range of technical applications, nickel oxide (NiO) is one of these well-known elements that has undergone substantial research. Characteristically, NiO is a well-known antiferromagnetic material possessing cubic structure [2-5]. Its electronic band gap is in between 3.6-3.8 eV which can prove to be tailor-made by reducing its particle size employing any synthesis route or by incorporating suitable foreign elements. Nickel oxide (NiO) is found to be one of the best host materials can accommodate foreign elements of different nature and hence, no surprise in its characteristic changes results for possessing entirely novel behavior and ensures its application demand. Significance of NiO nanomaterial is mainly because of its special characteristics like long-lasting, reusable for long periodic term, cost effective and narrow bandgap element.

* Corresponding author: ukloyola@gmail.com
<https://doi.org/10.15251/DJNB.2024.191.115>

Dopants from the I through V group of elements often make it easier to make a stable p-type NiO semiconductor. One of these metal oxides, Li, has been discovered to increase the lattice of the host material during incorporations, increasing the electrical resistivity and making them appropriate for the production of transparent conducting oxides, piezoelectric devices, and memory devices [6–9]. On contrary, the presence of Li can decrease the resistivity of NiO and leads to improve its electrochromic properties. It follows that the importance of comprehending how dopant concentration affects the outcome qualities is clear. Although, numerous methods such as hydrothermal method, Sol-gel are available to prepare NiO, co-precipitation method is found to be one of the suitable and cost effective methods can be chosen in the present work.

In the present work, amongst the scopes, exploration of dye degradation ability of the present samples is the primary one. Earlier studies reveal, rare earth metals are known for their ability to capture electrons, which helps to avoid the photo-generated electron-hole recombination. Electron trapping by europium ions, smaller particle size, more surface area, and increased surface roughness may all contribute to the improvement of photocatalytic activity.. Lithium is also one of such elements, gain interest for its incorporation with host element mainly because of its strong photocatalytic activity in organic pollutant degradation. Suppression of electron-hole pair recombination, in addition with significant content of oxygen vacancies, red transfer, and heavy absorption of OH ions on the catalyst surface, helps enough to increase in photocatalytic activity [10-14]. It is expected that incorporation of Li with NiO may lead to increase the Li+ content, resulting in electrocatalytic activity enhancement. Present work focuses on exploring the changes in the crystalline structure, optical and photocatalytic properties by virtue of Li incorporations with NiO. The synthesized nanoparticles are proposed to characterize by X-ray diffraction studies (XRD), Fourier transform infra-red spectroscopy (FTIR), Transmission electron microscopy (TEM) UV–visible spectroscopy CV and photocatalytic studies.

2. Materials and methods

2.1. Preparation of NiO doped Li nanoparticles

Without further purification, the co-precipitation process was used to create NiO nanoparticles utilizing high purity precursor chemicals (AR grade), such as $\text{Ni}(\text{NO}_3)_2 \cdot 6\text{H}_2\text{O}$ and sodium hydroxide (NaOH). The necessary amount of $\text{Ni}(\text{NO}_3)_2 \cdot 6\text{H}_2\text{O}$ (0.1 M) was first fully dissolved in deionized water, and then aqueous NaOH (0.8 M) solution was added drop by drop to it. The aqueous solution was then agitated for 6 hours at 80 °C, resulting in the production of a green precipitate. The precipitate was then repeatedly rinsed with ethanol and double-distilled water before being dried at 120 °C. The resultant material was then annealed at 600 °C for 5 hours. Finally, pure NiO nanoparticles were gathered and used for additional research. In the doped samples prepared NiO nano powder with admixture of lithium nitrate 2 mol%, using the deionized water as a solvent. The stoichiometric ratio of this preparation was 98 % and 2% mol of nickel oxide to NiO NPs. Using magnetic granulate, we have kept the solution well-protected to 8 hours while achieving complete dissolution. This solution has been dried and cleaned with ethanol and deionized water to keep contaminants from coming into touch with the nanoparticles mentioned. The precipitate was then heated to roughly 150 °C for three to four hours in a hot air furnace, where it quickly burned down. The agate mortar was then charity to crush the mixture into powder for additional analysis.

3. Results and discussion

3.1. X-Ray Diffraction studies

Figure 1 shows the X-ray diffraction patterns of Li doped NiO nanoparticles. According to the XRD spectrum, face-centered cubic NiO (FCC) with the space group $\text{Fm}\bar{3}\text{m}$ (225) was formed [15]. It is possible to relate the major diffraction peaks at (2) 37.34°, 43.32°, 62.9°, 75.4°, and 79.39° in perfect agreement with the crystal planes at (111), (200), (220), (311), and (222), respectively. The yield product of nanocrystalline NiO created using this process has no

contaminants, according to XRD. The emergence of distinct intensity peaks reveals the produced nanoparticles' crystalline structure. Using Bragg's equation, the lattice constant of NiO may be determined from the conspicuous peak (111):

$$a = d_{hkl} \sqrt{h^2 + k^2 + l^2}, \quad (1)$$

where the miller indices are (h, k, l). Both pure and NiO doped Li nanoparticles were found to have the same lattice constant for the (111) plane, which was reported to be 0.417 nm. The observed values closely match those of bulk NiO obtained from (JCPDS card number 04-0835), confirming the well-organized crystallinity of NiO. It's interesting to note that the yield NiO@Li nanoparticles' structure-oriented characteristics are unaffected by the incorporation of the Li ion. The line broadening measurement was used to estimate the average crystallographic size (D) of the NiO particles [16].

$$D = k\lambda/\beta \cos \theta \quad (2)$$

where the X-ray's wavelength, λ , is 1.54056 nanometers, FWHM stands for full width at half maximum, θ is the diffraction angle calculated from 2 values corresponding to the peak of highest intensity in the XRD pattern (200), and k is an empirical constant of 0.9. Table 1 lists the predicted average crystalline sizes of pure and NiO-doped Li nanosized particles together with the lattice constant a. NiO doped lithium nanoparticles have smaller crystalline sizes than pure NiO nanoparticles, as can be seen in Table 1. As a result, adding 0.1M Li inhibits nanoparticles from aggregating and creates a nucleation point for their proliferation [17]. In other words, the Li ion that is integrated into the nanoparticle structure plays the key job of the capping agent

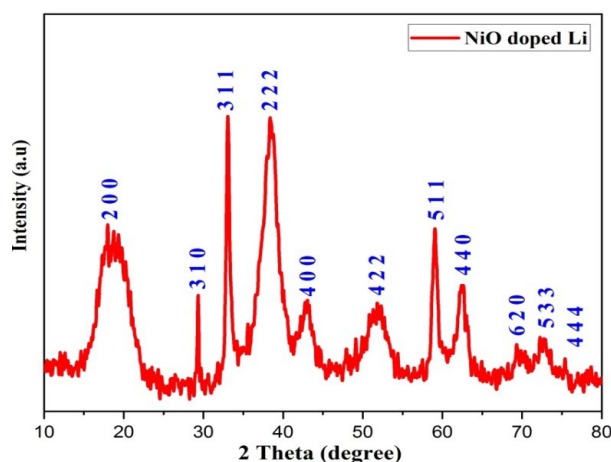


Fig.1. XRD patterns of NiO doped Li NPs.

$S/\tan \theta$ relates the distortion of strain-induced peak broadening and crystal flaws. Equation (2) has a remarkable quality in that it depends on the diffraction angle. While the W-H technique uses a $\tan \theta$ dependency, the Scherrer equation uses a $1/\cos \theta$ dependency. This finding demonstrated how the reflection broadening simultaneously induced microstructural changes brought on by a small crystallite size and microstrain. Williamson and Hall have been used to analyze the separations of size and strain broadening depending on various positions. The Scherrer equation and $S/\tan \theta$ are added to get the results that are shown below

$$\beta_{hkl} = \beta_s + \beta_D \quad (3)$$

The following sections detail how the modified W-H equation was used to calculate average particle size and microstrain in the current work.

$$\beta_{hkl} \cdot \cos\theta = k\lambda/D + 4\epsilon \cdot \sin\theta \quad (4)$$

The uniform deformation model equation, often known as equation (3), is a straight-line equation that takes the crystals' isotropic nature into account. Figure 2, a graphic illustrating the outcomes of the UDM analysis, was created using the data generated by equation (3). In this plot, a trending line drawn representing the variation of $\beta \cos\theta$ against $4\sin\theta$ for all the peaks of NiO with doped lithium and the correlation coefficient value of R^2 is calculated as 0.93543. Where equation (3) denotes UDM with the supposition that the stain is uniform along all crystallographic axes. The slope and y-intercept of the fitted line are used in the figure to determine strain and particle size, respectively. Calculations of the lattice parameters revealed that this strain might be brought on by lattice shrinkage.

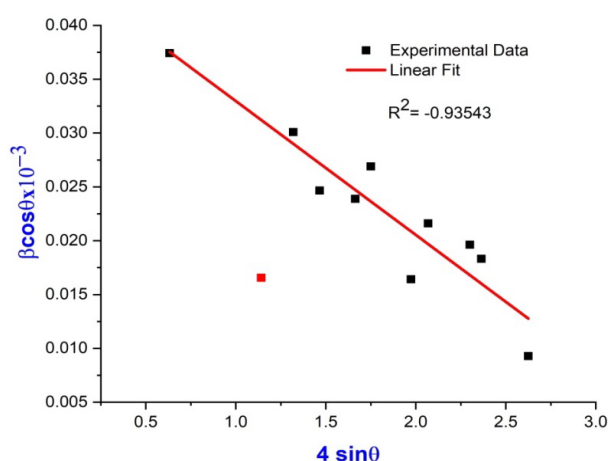


Fig.2. Williamson–Hall (W–H) plot for NiO@Li nanoparticles.

3.2. FTIR Spectra Analysis

The FTIR spectra of pure and NiO nanoparticles that have been annealed at 600 °C are shown in Figure 3. Spectra recorded between 4000 cm^{-1} and 400 cm^{-1} in the scanning range. Both of these spectra clearly show a number of important absorption peaks. Broad absorption band is observed to have appeared in both spectra between 3440 and 3459 cm^{-1} , which is attributed to O-H stretching vibrations. H-O-H bending vibrations can be attributed to a faint band seen close to 1630 cm^{-1} . Both of these functional vibrations make it clear that water molecules are present on the surface of NiO samples and that hydration has an impact on NiO nanoparticles. The stretching vibrations of the C-O and symmetric and asymmetric stretching vibrations of the O-bonds are responsible for the characteristic bands that were seen in the range of 1000-1500 cm^{-1} [18-20].

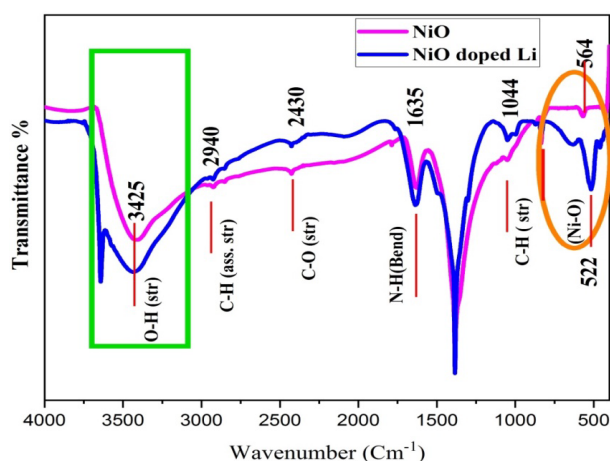


Fig.3. FT-IR spectrum of pure and doped NiO NPs.

3.3. UV–visible analysis

Observed UV–visible spectrum of Li free and incorporated NiO nanoparticles are given in Figure 4. In the scanning region of UV-Vis. wavelength from 200 to 800 nm, these two samples evident two different absorption edges as 232 and 245 nm respectively for Lithium free and incorporated NiO samples. As an evident, it confirms the changes in the bandgap value of NiO result of Li inclusions [21]. The following equation is typically used to estimate the absorption band gap (E_g):

$$\ln(Ah\nu) = \ln B + n(h\nu - E_g) \quad (5)$$

where A represents absorbance, B is a material-related constant, and n denotes either 2 or 1/2 for a direct transition or an indirect transition, respectively [22]. Where h is the photon energy. Therefore, by projecting the linear section of the $(h\nu)^n$ curve to zero, it is possible to determine the optical band gap for the absorption peak. The sample's $(h\nu)^2$ against h curve is depicted in Fig. 5a. According to estimates, the band gap of the NiO particles is 3.8 eV, which is lower than the band gap of bulk NiO (4.0 eV) [23]. The band gap energy of nanomaterials typically exhibits a blue shift, however the recently produced material had a red shift. This could be explained by the presence of chemical vacancies or flaws in the crystals, which would alter the electronic states in the band gap and reduce band gap energy [24]. When $n=1/2$, no linear relationship was discovered, indicating that the calcined NiO nanoparticles undergo a straight transition to semiconductivity at this energy [25]. Furthermore, it is widely known that when the grain size of semiconductor nanoparticles decreases, so does their energy band gap. Because of their short Bohr radius, there is no quantum confinement effect.

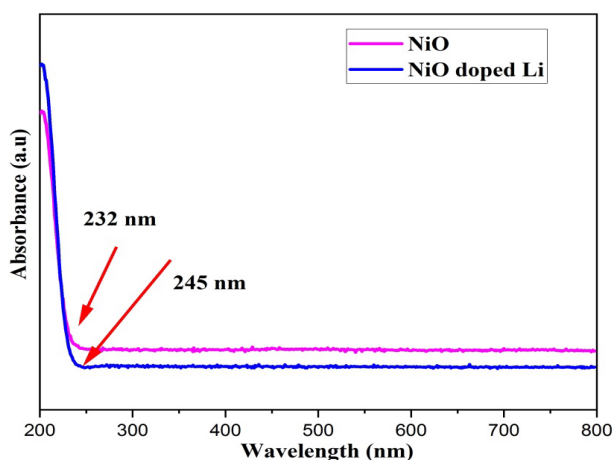


Fig. 4. UV-vis spectrum of pure and doped NiO NPs.

3.4. Transmission Electron Microscopy

The TEM images of pure and NiO doped Li nanoparticles that have been calcined are shown in Figure 6. As can be shown, generated NiO nanoparticles have weak agglomerations and a uniform distribution [26]. Nearly all of the particles are comparable in size, falling between 40 nm and less. The co-precipitation approach utilized in the present work is better suitable for the synthesis of nickel oxide nanoparticles because of the distribution of particles shown in the TEM picture. The effect of included Li as a capping agent was investigated using observed TEM data, which led to a considerable reduction in the size of the nanoparticles and an increase in their stability. This mechanism, which is responsible for the steric hindrance that keeps nanoparticles stable for months, involves the creation of a strong covalent connection between molecule chains and the surfaces of nanoparticles [27, 28]. Table 1 displays the obtained crystalline sizes from the TEM images. Data on crystalline sizes that were tabulated and those obtained from XRD peak broadenings correlated well

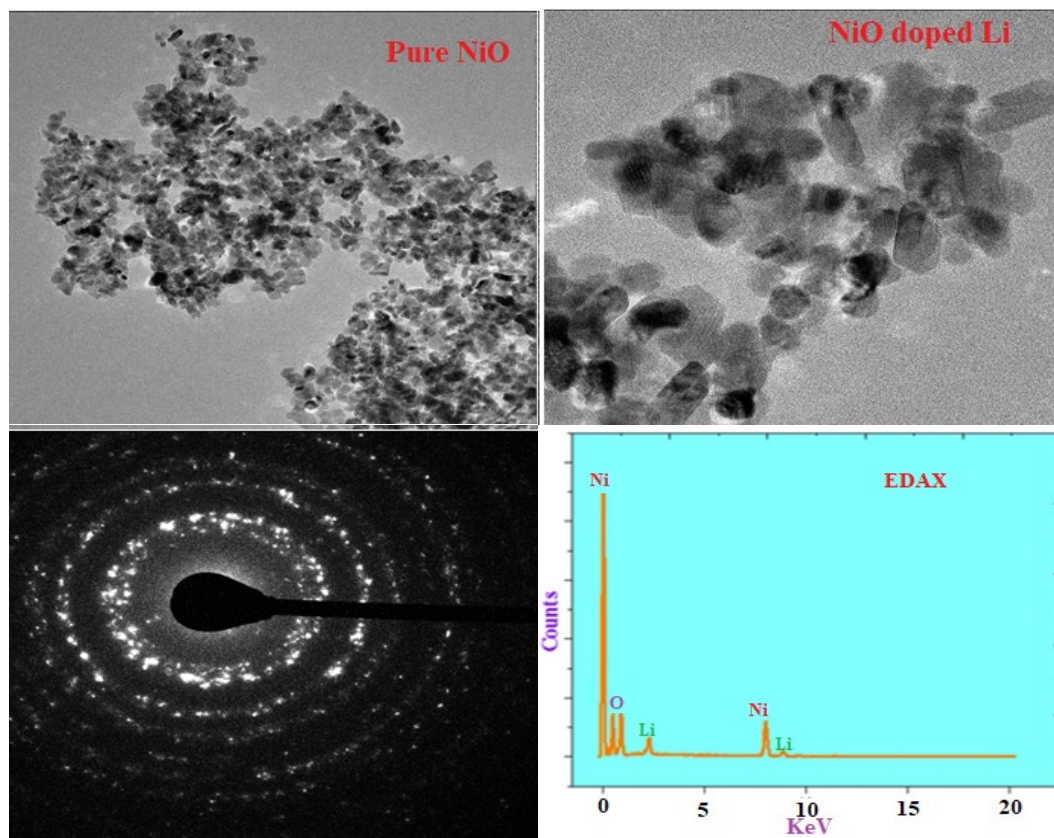


Fig. 6. TEM micrograph with EDAX spectrum of pure and doped NiO NPs.

3.5. Photocatalytic analyses

Organic dyes can be safely degraded by sunlight using the photodegradation process that uses nanomaterials, which releases H₂O and CO₂. By adding CO, the bandgap level of pure and doped NiO nanoparticles slowly decreases, indicating that they can be used as effective visible-light-driven photocatalysts. As a result, the catalytic analysis of NiO nanomaterial is assessed in relation to a hazardous organic dye called methylene blue (MB), among other things. Such analysis is important because it allows researchers to examine how effectively NiO nanomaterials are used to remediate wastewater. The photodegradation of the MB dye using NiO nanoparticles as a catalyst is shown in Fig. 7. Under UV illumination (125 W with maximal emission at 365 nm), the photocatalytic degradation of MB dye in an aqueous solution is studied. Under stirring, MB dye is mixed with a concentrated solution of 10 ppm NiO nanocatalyst. The experiment is conducted at room temperature in a photo reactor. The photoreactor's central irradiation source is an ultraviolet lamp with a wavelength of 365 nm. To keep the temperature between 25 and 30 °C, a continuous water flow has been set up. After 30 minutes of dark storage, the solution has reached adsorption equilibrium, at which point the spectrophotometer is used to measure the absorbance readings. The UV light is then turned on, and the sample's absorbance is measured every 30 minutes. The sample remains exposed to the UV light for 150 minutes. The formula [29] is used to determine each material's absorption percentage.

$$D(\%) = \frac{C_0 - C_t}{C_0} \times 100 \quad (5)$$

where the starting and final concentrations are C₀ and C_t, respectively. The studies are carried out to assess the impact of a catalyst combined with UV light on the degradation of MB dye. According to Figure 7, the intensity of MB dye's absorption is at its highest under low light conditions. The MB dye's absorption intensity gradually fades as time goes on. The fact that the MB dye solution turns colorless and the absorbance is extremely low after 2 hours suggests that

the pollutant is degraded under UV light during that time. After 2 hours of UV light irradiation, the deterioration efficiency is evaluated at 75%. The MB adsorption by the catalyst increased linearly when exposed to UV light. Li doped NiO nanoparticles alter MB dye adsorption, mostly due to the smaller crystallite size and higher surface area. The blue color of the MB dye solution changed to colorless after 150 minutes, demonstrating the NiO nanoparticles' potent catalytic activity. Absorption values considerably dropped every 30 minutes after that. Although, earlier reports states the photocatalytic performance of NiO nanoparticle synthesized by hydrothermal, sol-gel, thermal decomposition and green synthesis methods, etc., this work reveal how the photocatalytic efficiency of NiO which synthesized employing co-precipitation method, can be enhanced with the help of additive capping agent Li. The electron excitations from the valence band (VB) into the conduction band (CB) are enhanced by its lower E_g value of 1.53 eV. Lithium ions act as an electronic trapping center, which impacts how quickly e-h recombination occurs.

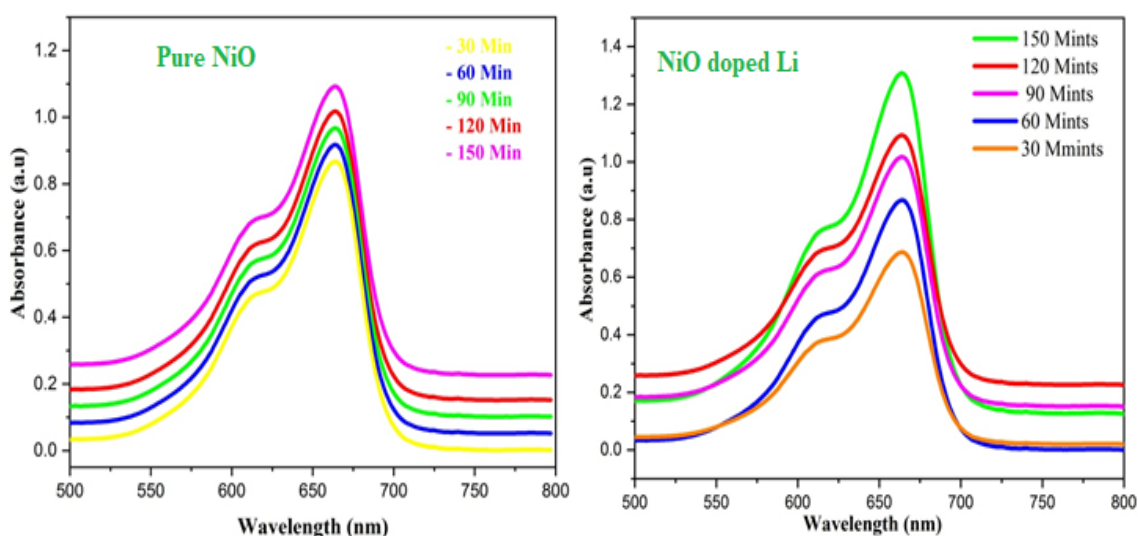


Fig. 7. UV-vis spectra during photocatalytic treatment of MB under UV-light irradiation of pure NiO doped Li nanoparticles.

3.6. Degradation mechanism

According to the theory of semiconductor photocatalysis, when rare earth ferrite's valence electrons are stimulated by light with a wavelength of 350–750 nm, they can produce a very active light hole–electron pair that improves its visible light catalytic performance. When compared to other catalysts, the NiO sample's photocatalytic activity can also be attributed to a number of factors, such as strong visible light absorption, uniform nanoparticle morphology with high specific surface area, and decreased charge carrier recombination. We outlined the potential photocatalytic degradation of dye by the produced materials shown in Fig. 10. We outlined a potential process for dye degradation by photocatalysis using the generated materials. Both n-type and p-type carriers are stimulated by simulated sunlight irradiation during the photodegradation process, producing electron hole pairs as a result. The photogenerated electron in the p-type NiO's conduction band (CB) will have no trouble moving to the n-type NiO's CB. The holes will go from Li (Eq. (6)) to the NiO valence band (VB). As a result, charge carrier separation is encouraged, which increases photocatalytic activity. Superoxide anions (O_2^-) are created when oxygen (O_2) dissolved in the solution interacts with the photogenerated electrons in the conduction band (Eq. (7)). As a result of their interaction with H_2O , the valence band's holes produce activated hydroxyl (OH^\cdot) radicals (Eq. (8)). These recently formed species are extremely reactive and have the ability to cause dye molecules to undergo CO_2 and H_2O conversions (Eq. (9)). According to other reports [30], the addition of NiO (p-type semiconductor) to the porous NiO (n-type semiconductor) matrix lowers the likelihood of photogenerated charge carriers recombining, increasing the photocatalytic activity. By producing a p-n junction that effectively separates electron hole pairs, NiO enhanced

the photocatalytic behavior. The inner electric field produced by the p-n region helped transport the photogenerated holes into NiO, which in turn prevented photogenerated electron hole pairs from recombining [31]. According to research by Fujita et al., adding metal oxide to NiO causes the development of a p-n junction in which an internal electric field appears at the metal oxide/NiO contact. This might lower the optical excitation's energy. As a result, the optical excitation's energy may be lowered and the unintended charge carrier recombination that is brought on by the photoexcitation of the NiO doped Li catalyst may be slowed [32]. The following equations could serve as a representation of the deterioration process



The production of OH radicals as a result of a high concentration of hydroxyl ions in the alkaline medium is a potential explanation for the accelerated photocatalytic degradation of MB at higher pH values, albeit, since the adsorption of dye was low and the surface area was only moderate (11.8 m² g⁻¹) [33]. The graph of $\ln(C/C_0)$ vs time, t , shown in figure 8 at various pH values was utilized to characterize the photocatalytic degradation rate of MB by using a condensed Langmuir-Hinshelwood (L-H) kinetic model (equation 10).

$$-\ln \frac{C}{C_0} = kt \quad (10)$$

The primary determinant of a semiconducting photocatalyst's photocatalytic activity is efficient charge separation. Thus, using the following empirical equations, it was crucial to establish the conduction band (CB) and valence band (VB) potentials of the NiO photocatalyst

$$E_{\text{VB}} = \chi + 0.5E_{\text{g}} - E^{\circ} \quad (11)$$

$$E_{\text{CB}} = E_{\text{VB}} - E_{\text{g}} \quad (12)$$

where E_{CB} is the conduction band edge potential, E_{VB} is the valence band edge potential, χ is the semiconductor's electronegativity, E° is the energy of free electrons on the hydrogen scale (4.5 eV), and E_{g} is the semiconductor's band gap energy.

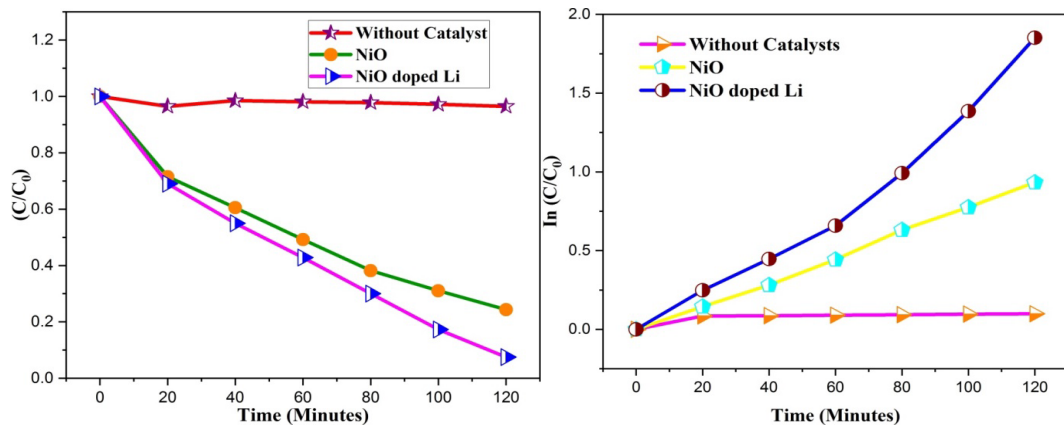


Fig. 8. Plot of degradation efficiency C/C_0 versus irradiation time of MB on NiO doped Li nanoparticles

3.7. Reproducibility of tests

The synthesized photocatalysts were examined to determine their reproducibility. All five samples were tested under the same conditions in which the samples led to attain complete MB degradation shown in figure 9. In all three experiments, the catalysts' performance was shown to be steady, followed by a modest decline in activity. Since the reuse of catalyst results in decreased photocatalytic behavior, as reported by numerous researchers, this decreasing response of photocatalytic activity is rather understandable. The results that were seen showed that the current samples performed satisfactorily, and they also supported the idea that these catalysts may be reused. Standard deviation is calculated using the same outcome.

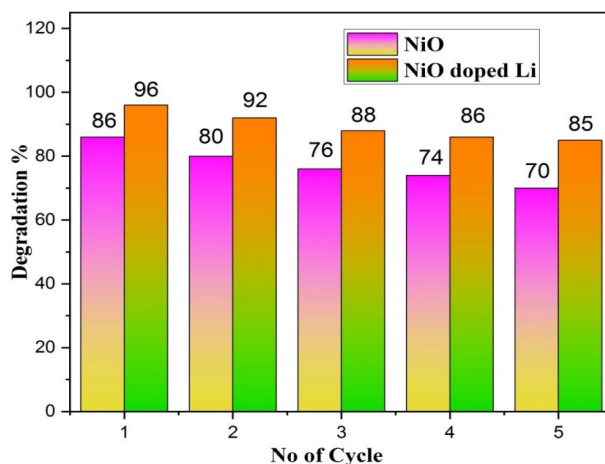


Fig. 9. Recycle efficiency of MB on NiO doped Li nanoparticles.

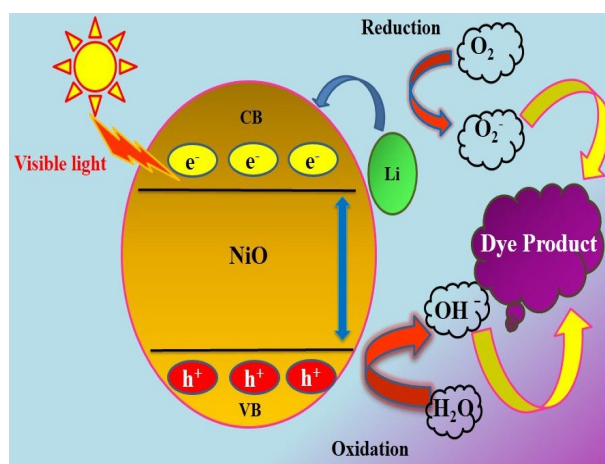


Fig. 10. Schematic representation of photocatalytic mechanism of MB dye using catalyst under visible light.

3.8. Cyclic voltammetry

In addition to other research, such UV-Visible spectroscopy, electrochemical approaches to explore the metallointercalation and coordination of metal ions and nanomaterials offer a useful supplement. Voltametric techniques have the potential to be used to study small molecules that are not susceptible to such methods due to weak absorption bands or because their electronic transitions overlap with those of the NiO molecule. It is possible to see combinations of many interacting species as well as multiple oxidation states of the same species at once. Shifts in peak potentials and the number of base pair sites involved in binding by intercalative, electrostatic, or

hydrophobic mechanisms can be used to calculate equilibrium constants (K) for the interaction of metal complexes with NPs [34–36]

Cyclic voltammograms (CV) produced in NiO and NiO@Li with increasing Cl content are shown in Fig. 11. Whatever the Cl concentration in the solution, the two peaks on the CV the nickel reduction and oxidation peaks seem to maintain the same form. At around 80 mV, copper ions on the gold-coated surface start to reduce from a NiO solution. That is consistent with response (1). 10 mA cm² is the limiting current density. The influence of the chloride ions on the copper reduction and oxidation pathways is demonstrated by comparing the anodic and cathodic peak morphologies on the voltammograms as a function of Cl concentration. The Ni⁺ reduction over-potential is 30 mV less than even the lowest concentration (50 ppm) applied. With increasing Cl content, an accelerating impact is shown. The increase in Cl causes the oxidation peak on the anodic half to climb, and the more Ni⁺ ions are reduced on the cathodic side, the more copper may be oxidized there. The copper deposit's formation and dissolution are both accelerated by Cl. The morphology of the anodic CVs slightly changed for the maximum chloride ion concentration, with the oxidation peak showing some bumps on both sides. The direct mass fluctuation that corresponds to the reported figure's voltammograms.

The curves clearly show a correlation between the current evolution on the voltammograms and NiO solution, as well as NiCl solutions with the lowest Cl concentrations (50 and 200 ppm). As soon as the deposition potential is reached, the continuous mass increase shows the thickening of the copper deposit, which slows down near the equilibrium potential. The mass of the deposited copper declines throughout oxidation until it reaches zero at the conclusion of the cyclic potential sweep. In the oxidation phase, the mass evolution has a "abnormal" appearance for the highest Cl concentration (500 ppm). From the start of the electrodeposited copper's dissolution, a mass increase (depicted with an arrow) rather than the anticipated mass drop is seen. This mass gain suggests that the dissolution is starting with a fresh process. The rate of mass transfer and the rate of charge transfer can be directly compared by using dm/dt rather than m [37–40]. According to the equation, the current is correlated with the rate of mass transfer based on the morphologies of the and voltamograms.

$$I \approx dm/dt \quad (13)$$

Regardless of the Cl content, a comparison of the cathodic portions of the two types of curves reveals a faradic deposition process of Ni⁺. When the Cl concentration is high (500 ppm), however, we observe a positive mass flux at the start of the deposit oxidation rather than a negative one. This Faradic oxidation, which results in a deposition rather than a dissolution process and was already mentioned in the previous paragraph, is better demonstrated in this presentation. We carried out some cyclic voltamograms, lowering the potential scan from 100 to +600 mV, to better understand this behavior. As a result, there is less electrodeposited copper, which makes it possible to demonstrate the anodic component of the CVs. The acquired CVs are displayed in Figure. Each CV has a single reduction peak. Copper is usually reduced in a single step (reaction 1). Ni⁺-free intermediate steps are not seen. Conversely, we found that the copper deposit disintegrated more slowly in the presence of Cl when the oxidation pathway from NiO only has one step. In that situation, the voltamograms show two or three twisted anodic peaks (A1, A2, A3). The first anodic peak "A" splits into peaks A1 and A2 as the Cl content rises, speeding up the dissolution process. A third peak can be seen at about +155 mV in potential. The concentration of chloride ions causes an increase in the three peaks' intensity. Two mass increases can be seen in the presence of a high Cl concentration on the m-E curves in Figure. On the NiO curve, P2 does not exist.

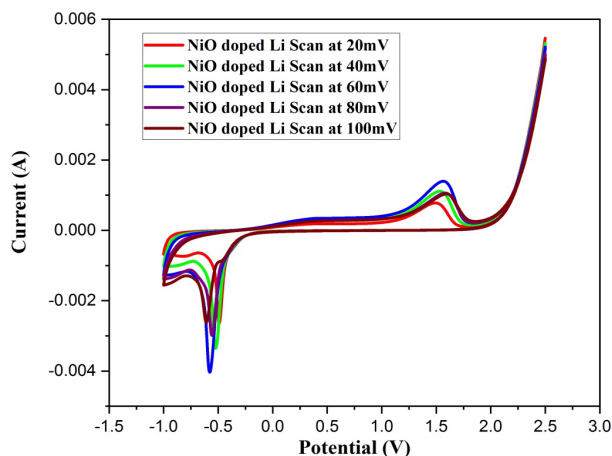


Fig. 11. Cyclic Voltammetry (CV) curves of NiO doped electrode with electrolytes at different scan rates; 20, 40, 60, 80, 100 mVs^{-1} within the potential window.

4. Conclusions

In the current study, pure and doped NiO nanoparticles are synthesized and characterized. The method's produced nanoparticles were annealed at 600 °C for four hours. The NiO@Li samples have an orthorhombic structure with an average grain size of 35.10 nm, according to the observed XRD analysis. The effective functions of the constituent elements correspond to NiO with great purity, according to the FT-IR and XRD data. The TEM and XRD examinations and the grain size of nickel oxide nanoparticles are closely correlated. Studies in the UV-visible range reveal an optical band gap of 3.8 eV, which denotes a red shift with size reduction. Pure NiO layers were granular with a fine structure, according to TEM images. The homogenous nanorod distribution throughout the entire surface characterizes the surface morphology of NiO and NiO doped Li nanoparticles. When compared to pure NiO nanoparticles, NiO containing Li nanoparticles in photocatalytic test had shown a considerable increase in the removal ratio of MB dye. The pores serve as locations where MB molecules are captured. Li nanoparticles were incorporated in NiO to limit the electron hole recombination and thus improve photocatalytic activity under visible irradiation. The best MB degrading efficiency was demonstrated by NiO with Li, reaching 96%. NiO sensitization, catalyst/dye contact period, and solution pH all have an impact on how much and how quickly MB is removed. The Elovich model was used to explain the kinetics of MB adsorption and degradation on NiO and NiO@Li in the current investigation. These investigations demonstrate the effectiveness of NiO doped Li hybrid nanocomposites as dye removal catalysts when exposed to visible light.

References

- [1] R. Ameta, M.S. Solanki, S. Benjamin, S.C. Ameta, Green Chem. Technol. (2018) 135-175; <https://doi.org/10.1016/B978-0-12-810499-6.00006-1>
- [2] M.J. Muñoz, D. Bahnemann, Sol. Energy. 77 (2004) 445-459; <https://doi.org/10.1016/j.solener.2004.03.031>
- [4] B.J. Rani, G. Ravi, R. Yuvakkumar, S. Ravichandran, F. Ameen, A. Al-Sabri, J. Sol-Gel Sci. Technol. 2018 892. 89 (2018) 500-510; <https://doi.org/10.1007/s10971-018-4886-5>
- [5] U.K. Panigrahi, P.K. Das, R. Biswal, V. Sathe, P.D. Babu, A. Mitra, P. Mallick, J. Alloys Compd. 833 (2020) 155050; <https://doi.org/10.1016/j.jallcom.2020.155050>
- [6] G. Sriakesh, A.S. Nesaraj, Ceram. Int. 42 (2016) 5001-5010; <https://doi.org/10.1016/j.ceramint.2015.12.013>

- [7] R.A.C. Amoresi, R.C. Oliveira, N.L. Marana, P.B. De Almeida, P.S. Prata, M.A. Zaghete, E. Longo, J.R. Sambrano, A.Z. Simões, *ACS Appl. Nano Mater.* 2 (2019) 6513-6526; <https://doi.org/10.1021/acsanm.9b01452>
- [8] C.N.C. Hitam, A.A. Jalil, *J. Environ. Manage.* 258 (2020) 110050; <https://doi.org/10.1016/j.jenvman.2019.110050>
- [9] K. Kaviyarasu, P.A. Devarajan, S.S.J. Xavier, S.A. Thomas, S. Selvakumar, *Journal of Materials Science & Technology* 28 (1), (2012), 15-20; [https://doi.org/10.1016/S1005-0302\(12\)60017-6](https://doi.org/10.1016/S1005-0302(12)60017-6)
- [10] V. Perumal, C. Inmozhi, R. Uthrakumar, R. Robert, M. Chandrasekar, S. Beer Mohamed, Shehla Honey, A. Raja, Fahd A. Al-Mekhlafi, K. Kaviyarasu, *Environmental Research*, 209, (2022), 112821; <https://doi.org/10.1016/j.envres.2022.112821>
- [11] K. Kasinathan, J. Kennedy, M. Elayaperumal, M. Henini, M. Malik, *Scientific reports* 6 (1), 1-12, 2016; <https://doi.org/10.1038/srep38064>
- [12] R. M. Surya, S. Mauliddiyah, D. O.B. Apriandanu, Sudirman, Y. Yulizar, *Chemosphere*, 304 (2022)135125; <https://doi.org/10.1016/j.chemosphere.2022.135125>
- [13] J. Al Boukhari, L. Zeidan, A. Khalaf, R. Awad, *Chem. Phys.* 516 (2019) 116-124; <https://doi.org/10.1016/j.chemphys.2018.07.046>
- [14] S. Agrawal, A. Parveen, A. Azam, *J. Lumin.* 184 (2017) 250-255; <https://doi.org/10.1016/j.jlumin.2016.12.035>
- [15] H. Abbas, K. Nadeem, H. Krenn, M. Kostylev, J. Hester, A.T. Murdock, S. Yick, I. Letofsky-Papst, C. Ulrich, *Nanotechnology*. 31 (2020) 475701; <https://doi.org/10.1088/1361-6528/abaf23>
- [16] M. Chandrasekar, S. Panimalar, R. Uthrakumar, M. Kumar, M.E. Raja Saravanan, G. Gobi P. Madheswaran, C. Inmozhi, K. Kaviyarasu, *Materials Today: Proceedings*, 36, (2021), 228-231; <https://doi.org/10.1016/j.matpr.2020.03.228>
- [17] M.V. Arularasu, M. Anbarasu, S. Poovaragan, R. Sundaram, K. Kanimozhi, C. Maria Magdalane, K. Kaviyarasu, F.T. Thema, Douglas Letsholathebe, Genene T. Mola, M. Maaza, *Journal of nanoscience and nanotechnology* 18 (5), (2018), 3511-3517; <https://doi.org/10.1166/jnn.2018.14658>
- [18] S. Panimalar, R. Uthrakumar, E. Tamil Selvi, P. Gomathy, C. Inmozhi, K. Kaviyarasu, J. Kennedy, *Surfaces and Interfaces* 20, (2020) 100512; <https://doi.org/10.1016/j.surfin.2020.100512>
- [19] Amal George, D. Magimai Antoni Raj, X. Venci, A. Dhayal Raj, A. Albert Irudayaraj, R.L. Josephine, S. John Sundaram, Amal A. Al-Mohaimed, Dunia A. Al Farraj, Tse-Wei Chen, K. Kaviyarasu, *Environmental Research*, 203, (2022) 111880; <https://doi.org/10.1016/j.envres.2021.111880>
- [20] L.S. Nair, D. Chandran, V.M. Anandakumar, K. R. Babu, *Ceram. Int.* 43 (2017) 11090-11096; <https://doi.org/10.1016/j.ceramint.2017.05.155>
- [21] K.V. Chandekar, Mohd. Shkir, A. Khan, M.A. Sayed, N. Alotaibi, T. Alshahrani, H. Algarni, S. AlFaify, *J. Mater. Res. Technol.* 15 (2021) 2584-2600; <https://doi.org/10.1016/j.jmrt.2021.09.072>
- [22] G. Bharathy, P. Raji, *J. Mater. Sci. Mater. Electron.* 28 (2017) 17889-17895; <https://doi.org/10.1007/s10854-017-7730-8>
- [23] K.N. Patel, M.P. Deshpande, K. Chauhan, P. Rajput, V.P. Gujarati, S. Pandya, V. Sathe, S.H. Chaki, *Adv. Powder Technol.* 29 (2018) 2394-2403; <https://doi.org/10.1016/j.apt.2018.06.018>
- [24] S. Panimalar, S. Logambal, R. Thambidurai, C. Inmozhi, R. Uthrakumar, Azhaguchamy Muthukumaran, Rabab Ahmed Rasheed, Mansour K. Gatasheh, A. Raja, J. Kennedy, K. Kaviyarasu, *Environmental Research*, 205, (2022) 112560; <https://doi.org/10.1016/j.envres.2021.112560>
- [25] A. Raja, K. Selvakumar, P. Rajasekaran, M. Arunpandian, S. Ashokkumar, K. Kaviyarasu, S. Asath Bahadur, M. Swaminathan, *Colloids and Surfaces A: Physicochemical and Engineering Aspects*, 564, (2019), 23-30; <https://doi.org/10.1016/j.colsurfa.2018.12.024>
- [26] V. Perumal, A. Sabarinathan, M. Chandrasekar, M. Subash, C. Inmozhi, R. Uthrakumar, Abdulgalim B. Isaev, A. Raja, Mohamed S. Elshikh, SaedahMusaedAlmutairi, K. Kaviyarasu,

- Fuel, 324, (2022), 124599; <https://doi.org/10.1016/j.fuel.2022.124599>
- [27] S. Panimalar, M. Chandrasekar, S. Logambal, R. Uthrakumar, C. Inmozhi, *Materials Today: Proceedings*, 56, (2022), 3394-3401; <https://doi.org/10.1016/j.matpr.2021.10.335>
- [28] M. Chandrasekar, M. Subash, V. Perumal, S. Panimalar, S. Aravindan, R. Uthrakumar, C. Inmozhi, Abdugalam B. Isaev, SudhakarMuniyasamy, A. Raja, K. Kaviyarasu, *Separation and Purification Technology*, 294, (2022), 121189; <https://doi.org/10.1016/j.seppur.2022.121189>
- [29] M. Chandrasekar, M. Subash, S. Logambal, G. Udhayakumar, R. Uthrakumar, C. Inmozhi, Wedad A. Al-Onazi, Amal M. Al-Mohaimeed, Tse-Wei Chen, K. Kanimozhi, *J. King Saud Uni. - Sci.*, 34, (3), (2022), 101831; <https://doi.org/10.1016/j.jksus.2022.101831>
- [30] C. Thangamani, P. V. Kumar, K. Gurushankar, K. Pushpanathan, *J. Mater. Sci. Mater. Electron.* 2020 3114. 31 (2020) 11101-11112; <https://doi.org/10.1007/s10854-020-03659-2>
- [31] S. Sankar, S.K. Sharma, N. An, H. Lee, D.Y. Kim, Y. Bin Im, Y.D. Cho, R.S. Ganesh, S. Ponnusamy, P. Raji, L.P. Purohit, *Optik (Stuttg)*. 127 (2016) 10727-10734; <https://doi.org/10.1016/j.ijleo.2016.08.126>
- [32] C. Thangamani, P. Vijaya Kumar, K. Gurushankar, K. Pushpanathan, *J. Mater. Sci. Mater. Electron.* 2020 3114. 31 (2020) 11101-11112; <https://doi.org/10.1007/s10854-020-03659-2>
- [33] J. Liu, H. Wang, R. Ye, P. Jian, L. Wang, *Journal of Colloid and Interface Science* 585 (2021) 61-71; <https://doi.org/10.1016/j.jcis.2020.11.069>
- [34] N. Geetha, S. Sivaranjani, A. Ayeshamariam, M. Siva Bharathy, S. Nivetha, K. Kaviyarasu, M. Jayachandran, *Journal of Advanced Microscopy Research* 13 (1), (2018) 12-19; <https://doi.org/10.1166/jamr.2018.1352>
- [35] S. Panimalar, M. Subash, M. Chandrasekar, R. Uthrakumar, C. Inmozhi, Wedad A. Al-Onazi, Amal M. Al-Mohaimeed, Tse-Wei Chen, J. Kennedy, M. Maaza, K. Kaviyarasu, *Chemosphere*, 293, (2022), 133646; <https://doi.org/10.1016/j.chemosphere.2022.133646>
- [36] A.M. Amanulla, C.M. Magdalane, S. Saranya, R. Sundaram, K. Kaviyarasu, *Surfaces and Interfaces* 22, (2021) 100835; <https://doi.org/10.1016/j.surfin.2020.100835>
- [37] A. George, A. Dhayal Raj, A. Albert Irudayaraj, R.L. Josephine, X. Venci, S. John Sundaram, R. Rajakrishnan, P. Kuppusamy, K. Kaviyarasu, *Environmental Research*, 211, (2022), 112970; <https://doi.org/10.1016/j.envres.2022.112970>
- [38] A. Kumar, L. Rout, L. S. K. Achary, A. Mohanty, J. Marpally, P. K. Chand, and P. Dash, *AIP Conf. Proc.* 1724, (2016); <https://doi.org/10.1063/1.4945147>
- [39] R. Abinaya, J. Archana, S. Harish, M. Navaneethan, S. Ponnusamy, C. Muthamizhchelvan, M. Shimomura, Y. Hayakawa, *RSC Adv.* 8, (2018), 26664; <https://doi.org/10.1039/C8RA02560F>
- [40] C.M. Magdalane, G.M.A. Priyadharsini, K. Kaviyarasu, A.I. Jothi, G.G. Simiyon, *Surfaces and Interfaces*, 25, (2021) 101296; <https://doi.org/10.1016/j.surfin.2021.101296>